Can Meandering Flows in Shallow Rectangular Reservoirs Be Modeled with the 2D Shallow Water Equations?

Yann Peltier[1], Sébastien Erpicum[2], Pierre Archambeau[3], Michel Pirotton[4], Benjamin Dewals[5]

[1]Postdoctoral Researcher, University of Liege (ULg) – ArGEnCo Department, Research Group of Hydraulics in Environmental and Civil Engineering (HECE), Chemin des Chevreuils 1, Bat B52/3 +1, B-4000, Liège, Belgium. E-mail: Y.Peltier@ulg.ac.be (corresponding author)
[2]Research Associate, University of Liege (ULg) – ArGEnCo Department, Research Group of Hydraulics in Environmental and Civil Engineering (HECE), Chemin des Chevreuils 1, Bat B52/3 +1, B-4000, Liège, Belgium. E-mail: S.Erpicum@ulg.ac.be
[3]Research Associate, University of Liege (ULg) – ArGEnCo Department, Research Group of Hydraulics in Environmental and Civil Engineering (HECE), Chemin des Chevreuils 1, Bat B52/3 +1, B-4000, Liège, Belgium. E-mail: pierre.archambeau@ulg.ac.be
[4]Professor, University of Liege (ULg) – ArGEnCo Department, Research Group of Hydraulics in Environmental and Civil Engineering (HECE), Chemin des Chevreuils 1, Bat B52/3 +1, B-4000, Liège, Belgium. E-mail: michel.pirotton@ulg.ac.be
[5]Associate Professor, University of Liege (ULg) – ArGEnCo Department, Research Group of Hydraulics in Environmental and Civil Engineering (HECE), Chemin des Chevreuils 1, Bat B52/3 +1, B-4000, Liège, Belgium. E-mail: B.Dewals@ulg.ac.be

Abstract

In this article, the ability of the 2D shallow water equations to model meandering flows in shallow rectangular reservoirs is discussed. Four meandering flows, of various shallowness, were modelled using the academic flow model WOLF 2D, which includes a depth-averaged k-ε model accounting for the horizontal and vertical turbulent length-scales. The bottom friction was modelled with the Colebrook-White formula and different roughness heights were considered. A Proper Orthogonal Decomposition (POD) was applied to the simulation results to extract the behaviour of the main structures responsible for the meandering flow. The same POD analysis was also performed for the reference experimental flow fields, obtained by Large-Scale Particle Image Velocimetry. The first two POD modes obtained from the numerical simulations assuming a smooth bottom are in good agreement with the experimental modes in terms of energy, as well as temporal and spatial variations, whatever the shallowness. In contrast, the remaining simulated modes are not well rendered. The effect of an increased roughness height in the simulations is finally discussed. It leads to an

improved reproduction of the first two modes and of the following modes, except when significant viscous effects govern in the flow.

Keywords: Shallow rectangular reservoir, meandering jet, Proper Orthogonal Decomposition, shallowness, friction modelling, shallow water equations

Introduction

Shallow rectangular reservoirs are common structures in natural and built environments. They are used as storage reservoirs (flood-control, hydropower) or as settling reservoirs to trap pollutants and/or sediments (stormwater treatment, protection of irrigation systems).

In their studies, Dufresne *et al.* (2010a), Dufresne *et al.* (2012) and Peltier *et al.* (2013) emphasized that the optimal management of reservoirs (in terms of sediment transport and water storage) cannot be achieved without the detailed knowledge of the complex flow fields developing in such reservoirs. Indeed, regions with distinct mean velocities occur and large-scale horizontal coherent structures develop in the flow (Camnasio *et al.*, 2011, Dewals *et al.*, 2008, Dufresne *et al.*, 2010b, Kantoush *et al.*, 2008, Peltier *et al.*, 2014a, b). The flow fields in shallow rectangular reservoirs can be classified into four different flow patterns (Peltier *et al.*, 2014a), depending on the Froude number at the reservoir inlet, F, and on the geometry of the reservoir, characterized by the shape factor defined by Dufresne *et al.* (2010b) as $\mathsf{SF} = L/\Delta B^{0.6}b^{0.4}$ (*L* the reservoir length, *b* the width of the inlet channel and ΔB the width of the sudden expansion). For $\mathsf{SF} < 6.2$, the flow is symmetric and the jet remains straight when $\mathsf{F} < 0.21$; whereas it meanders for $\mathsf{F} > 0.21$ (Peltier *et al.*, 2014a). When $\mathsf{SF} > 8.1$, the flow is asymmetric whatever the Froude number and the jet impinges one or several times the side walls. Finally, for $\mathsf{F} > 0.21$ and $6.2 < \mathsf{SF} < 8.1$, the flow pattern is unstable and randomly switches between symmetric and asymmetric configurations, the jet being either straight or

meandering.

The hydraulic conditions and the geometries leading to symmetric and asymmetric flows are now relatively well documented in the literature (Aloui and Souhar, 2000, Camnasio *et al.*, 2011, Canbazoglu and Bozkir, 2004, Dufresne *et al.*, 2010b, Kantoush *et al.*, 2008, Mullin *et al.*, 2003, Oca and Masaló, 2007) and numerical models have demonstrated their ability to reproduce such flow features (Camnasio *et al.*, 2013, Dewals *et al.*, 2008, Dufresne *et al.*, 2011, Khan *et al.*, 2013, Peng *et al.*, 2011, Stovin and Saul, 2000). By contrast, very few experimental and numerical studies dealt with meandering flows in shallow rectangular reservoirs (Camnasio *et al.*, 2012, Kantoush, 2008, Peltier *et al.*, 2014a, b). As highlighted by Peltier *et al.* (2014b) by using a Proper Orthogonal Decomposition, the meandering jet is constituted by large-scale energetic turbulent structures, which contribute to increase the lateral momentum transfer between the jet and the rest of the flow (Chen and Jirka, 1999). When considering sediment transport in a shallow rectangular reservoir, this additional transfer of momentum is responsible for a wider spreading of the sediments on both sides of the jet compared to a configuration without meandering jet (Peltier *et al.*, 2013). This results in a significant rise in the overall trapping efficiency of the reservoir. However, this aspect is not taken into account in the current practice of reservoir design, as the standard approaches are mostly based on geometrical relationships alone. Serious price over-costs in the reservoir management may be avoided by a better consideration of the physics at the design stage, particularly through the use of numerical flow models. Therefore, assessing the predictive capacity of operational numerical models to simulate these meandering flows is of high practical relevance.

In the present article, we discuss the ability of the academic numerical model WOLF 2D (Dewals *et al.*, 2008), based on the shallow water equations, to reproduce meandering jets in shallow rectangular reservoir. The four flow configurations detailed in Peltier *et al.* (2014b)

were numerically modelled using WOLF 2D with a k-ε model accounting for two different turbulent length-scales (Erpicum *et al.*, 2009): the horizontal turbulence mixing is modelled by two additional transport equations (k and ε), while the vertical turbulence mixing is treated with an algebraic model (Elder formula). As the meandering jets are influenced by the bottom friction (Peltier *et al.*, 2014a), we also tested three different roughness heights. As the meandering flows are unsteady flows, experimental and numerical results were compared using a Proper Orthogonal Decomposition (Holmes *et al.*, 2012, Peltier *et al.*, 2014b) of the fluctuating velocity fields. Six major parameters characterizing the meandering behaviour were extracted from this analysis: the mean fluctuating kinetic energy distribution of the POD modes, the mean total fluctuating kinetic energy, the frequency and the mean amplitude of the first four temporal POD coefficients, as well as the longitudinal and lateral extensions of the first four spatial POD modes.

Experiments

Experimental setup and data-set

The experiments were carried out in a flume at the laboratory of engineering hydraulics of the University of Liege (ULg), Belgium. The experimental setup is shown in Figure 1 and a complete description of the experimental facility is provided by Peltier *et al.* (2014a) and Peltier *et al.* (2014b). The inlet and outlet channels are respectively 2 m and 1.5 m long. The dimensions of the reservoir were selected based on the criteria of Peltier *et al.* (2014a) for the occurrence of meandering flows in shallow rectangular reservoirs (SF < 6.1 and $F = U_{in} / \sqrt{gH} > 0.21$ with U_{in} the mean velocity at the inlet and g the gravity acceleration). The width of the inlet and outlet channels was set to 0.08 m. The reservoir length, L, was equal to 1 m and the width of the sudden expansion, ΔB, was chosen equal to 0.45 m. The discharges and the water depths were selected to obtain the desired Froude numbers and for

covering a broad range of friction numbers, $\mathsf{S} = f\Delta B / 8H$ (f the Darcy-Weisbach coefficient) (Chu *et al.*, 1983). In each experiment, the discharge, Q, was regulated to be kept constant. The water depth, H, was measured in three positions in the reservoir using an ultrasonic probe and was constant to the measurement uncertainty (1% of H). Their values are summarized in Table 1 together with the corresponding friction and Froude numbers. The Reynolds number in the inlet channel, $\mathsf{R} = U_{in}D / \nu$ (D the hydraulic diameter of the inlet channel and ν the kinematic viscosity of the water at 20°C), is also given in Table 1. It ranges between 4,766 and 24,267, which means that the jet can be considered as turbulent, but the flows are hydrodynamically smooth and some viscous effects may be expected.

As demonstrated by Peltier *et al.* (2014a), the characteristic lengths and frequency of the meandering jet show a strong dependence on the friction number S, which is an indicator of the shallowness of the flow. Depending on the value of S, different types of structures develop in the flow and affect the meandering of the jet (Peltier *et al.*, 2014b). The four different flow-cases considered here are named according to their friction regime, as defined by Chu *et al.* (2004). The turbulence-scale in the flow-case F ($\mathsf{S} = 0.18$) is mainly driven by the water depth and the bed friction has a stabilizing effect on the development of the structures (Chu and Babarutsi, 1988). This type of flow belongs to the "frictional" regime. In contrast, the turbulence scale is mostly driven by the horizontal length-scale, *i.e.* the sudden expansion width ΔB, for flow-case NF ($\mathsf{S} = 0.03$), which belongs to the "non-frictional" regime. The transition between the frictional and the non-frictional cases was found for S in-between 0.05 and 0.1 for sudden enlargements (Chu *et al.*, 2004). For meandering flows, Peltier *et al.* (2014a) indicate that a transition was observed around $\mathsf{S} = 0.07$. The flow case corresponding to $\mathsf{S} = 0.10$, is therefore referred as "frictional close to transition" (FT), while the flow case corresponding to $\mathsf{S} = 0.06$ is called "non-frictional close to transition" (NFT).

In the present paper, x, y and z designate the streamwise, spanwise and vertical directions of the Cartesian frame of reference; $x = 0$ immediately downstream from the inlet channel and $y = 0$ at the right bank of the reservoir. $z = 0$ at the bottom of the reservoir.

Velocity measurements

In the experiments, only the surface flow was reasonably accessible. The surface dynamics was therefore estimated using the surface velocity fields measured by Large-Scale Particle Image Velocimetry (LSPIV)Peltier *et al.* (2014b). This assumption was supported by the measurements of Rowland *et al.* (2009), who observed in a similar configuration (acrylic bed, R = 27,000, *H/B* = 0.2, with *H* constant in the reservoir) that the characteristics of the jet near the free surface are close to those of the mid-flow. This assumption is also supported by Peltier *et al.* (2013) and Mariotti *et al.* (2013), who showed a remarkable agreement between the measured surface characteristics of the jet and those predicted by a depth-averaged flow model (based on the shallow water equations). These results indeed suggest that the measured surface velocity fields are fairly representative of the large-scale instabilities. Some discrepancies between experiments and numerical modelling may nonetheless arise as a result of vertical secondary currents influencing the vertical distribution of velocity until x/H = 10 (Foss and Jones, 1968, Holdeman and Foss, 1975) and bottom generated turbulence that affects the flow close to the bottom.

Sawdust of 2 mm in diameter was used as seeding material in experiments. The sawdust was introduced at the surface of the flow, 3 m upstream from the converging zone (Figure 1), i.e. 5 m upstream from the reservoir inlet. The sawdust was regularly added to the surface so that a homogenous zone of 3 m × *B* of sawdust was advected into the reservoir. The video sequence used for the LSPIV calculation started as soon as the surface was homogenously occupied by the sawdust. A region of 1 m², containing the entrance of the reservoir (Figure

1), was video recorded at a rate of 25 Hz during 6 min using a commercial video-camera (Canon$^©$ HD-HG20). The recorded images were corrected for deformations and were orthorectified so that one pixel was equal to a square of 1 mm side. Using a LSPIV code based on the work of Hauet *et al.* (2008) and Hauet (2009), the surface velocity fields were worked out every centimetre along the *x* and *y* direction. The resulting velocity fields were finally corrected and low-pass filtered (Peltier *et al.*, 2014b).

Numerical modelling

WOLF 2D

The numerical modelling was performed using the academic model WOLF 2D developed at the University of Liege. It solves the shallow-water equations (Dewals *et al.*, 2008) by means of a finite volume scheme. The model was earlier validated for simulating flows in shallow reservoirs (Camnasio *et al.*, 2013, Dewals *et al.*, 2008, Dufresne *et al.*, 2011, Peltier *et al.*, 2013).

Second-order space accuracy is obtained by means of linear reconstruction at cells interfaces, combined with a slope limiter. The convective fluxes are computed by a Flux Vector Splitting (FVS) method (Erpicum *et al.*, 2010). This FVS method requires low computational cost, offers the advantage of being Froude-independent and enables a well-balanced discretization of the bottom slope term. The time integration is performed by means of a 3-step third-order accurate Runge-Kutta algorithm. The time step is adaptive and is constrained by the Courant-Friedrichs-Lewy (CFL) stability condition.

The turbulent fluxes were evaluated by means of a centred scheme and a two length-scale depth-averaged turbulence model accounting for horizontal and vertical turbulent mixing (Babarutsi and Chu, 1998, Erpicum *et al.*, 2009). A depth-averaged k-ε model was used for modelling the horizontal mixing, while the vertical mixing, associated to the bottom-

generated turbulence, the length-scale of which is of the order of magnitude of the water depth H, was treated with an algebraic model (Elder formula Model: $v_{T,3D} = 0.08Hu_*$, v_t the eddy viscosity related to the vertical turbulent mixing and u_* the friction velocity). Though the k-ε model may not model the near-wall flow satisfactorily, it was preferred as k-ε model remains the most widely used two-equation turbulence closure model. The coefficients in the turbulence model were kept at their standard value (Erpicum *et al.*, 2009).

The standard Colebrook-White formula was used for modelling the friction (Camnasio *et al.*, 2013, Dufresne *et al.*, 2011).

Numerical data-set

The simulations were conducted using three roughness heights. The bottom and side-walls were first assumed to be smooth ($k_s = 0$ mm). The influence of the friction was next investigated based on additional simulations considering mildly rough ($k_s = 0.1$ mm) or rough ($k_s = 1$ mm) bottom conditions. In the simulation, the 2 m-long inlet channel (Figure 1) was reproduced to keep the injection in the reservoir as close as possible to the experimental configuration (Peltier *et al.*, 2014b). The discharge read on the flow-meter, with an accuracy of ±0.025 L/s, was prescribed as inflow condition upstream from the inlet channel. As prescribed by Dewals *et al.* (2008), a slightly uneven transverse distribution of the inflow discharge was used as a seed for asymmetry. The disturbance varied linearly from -1% to +1% across the inflow section. The water depth measured 13 cm downstream from the outlet of the reservoir was prescribed as downstream boundary condition.

For each simulation, the initial condition and the boundary conditions were obtained from an unsteady computation performed until temporally and spatially stable oscillations of the jet were obtained. Once this regime state was reached, the results were recorded at a rate of 25Hz to enable direct comparisons with the experiments. The grid spacing was set to

0.01 m, and with a CFL value of 0.2, the time step was between 1.5×10^{-3} s and 4×10^{-3} s, the resulting sampling being actually equal to 25 Hz ± 2.3 Hz. The choice of the grid spacing was guided by the grid independence tests presented in Dufresne *et al.* (2011) and Camnasio *et al.* (2012), which are based on the grid convergence index introduced by Roache (1994). Although Dufresne *et al.* (2011) highlighted the great sensitivity of reattaching flows to the grid resolution, Camnasio *et al.* (2012) showed that the main characteristic frequency of the meandering jet is weakly affected.

For comparing the numerical results with experiments, we considered that the depth-averaged velocities were close to the velocity at the free surface in most parts of the reservoir. No surface coefficient accounting for the difference between the surface velocity and the depth-averaged velocity was applied on the experimental velocity fields (Le Coz *et al.*, 2010).

Results

The meandering jet is characterised by spatial and temporal periodical oscillations. These oscillations are the sum of the contribution of various sizes of energetic coherent structures, which are convected in the flow and are mainly generated by the geometry of the reservoir (Peltier *et al.*, 2014a, b). As a consequence, the standard flow variables (velocity fields, Reynolds shear stresses …) usually used for describing and comparing flows together are not the most appropriate here.

Therefore, the description of the flows is based there on the results of a Proper Orthogonal Decomposition (POD) of the experimental and numerical fluctuating velocity fields (Berkooz *et al.*, 1993, Holmes *et al.*, 2012). The POD enables the identification of the flow structures contributing most to the flow energy (Brevis and García-Villalba, 2011), gives their temporal evolutions and sorts the modes by decreasing energy (see appendix). This decomposition is optimal in average on the time interval covered by the data (Couplet *et*

al., 2003), *i.e.* there is no better decomposition for discriminating the structures with respect to their respective energy contributions (Cavar and Meyer, 2012, Perrin *et al.*, 2007).

In the present work, the snapshot method (Sirovich, 1987) was applied to 9,000 flow fields extracted from the experimental measurements and numerical simulation results of each of the flow-cases listed in Table 1 (see appendix for the description of the snapshot method). The size of the computation grid equals ~10,000 points in each case. The area of analysis is limited to the reservoir and does not extend to the inlet and outlet channels (Figure 1). In the experiments, the velocity field was not available close to the downstream end of the reservoir, because of the position of the video camera.

Temporal coefficients

The temporal coefficients calculated with Eq. 4 are represented in Figure 2 for the flow-case FT. For the first two modes, results from experiments and numerical simulations are very similar, in terms of both frequency and amplitude. Moreover, the phase-shift between the temporal coefficients of modes 1 and 2 is the same for the simulation and for the experiments. This indicates that the modes of the computed results are representative of the same type of coherent structures as in the experiments (Rempfer and Fasel, 1994). In contrast, for the next modes, significant differences are observed. In all the experiments, Peltier *et al.* (2014b) observed that the third mode represents a low-motion of the flow and is probably due to the experimental set-up. Here, in the simulations, this mode was obviously not observed. As a consequence, we do not consider this mode in the comparisons and the fourth and fifth experimental modes were systematically compared with the third and fourth modes of the numerical simulations. This comparison reveals that although the amplitudes of the temporal coefficients are comparable, the frequencies are different. Nonetheless, a constant phase-shift between the consecutive modes is observed in both the experimental and

numerical results. This indicates that, as experimentally observed, coherent structures are also rendered by the numerical model for these modes. The experimental observations emphasized that, from $m = 6$, the POD modes had low effects on the flow. We therefore restrain the present analysis to the four first modes for the numerical simulations.

The frequencies and the mean amplitudes of the first four temporal coefficients of the numerical simulations are summarised in Table 2 for all flow-cases. For the modes 1 and 2, the frequencies match exactly only for the flow-case FT. They are overestimated by 49% for F and by 39% for NFT, and they are underestimated by 28% for NF. Concerning the mean amplitudes, they are between -35% and 35 % of the experimental amplitudes. For the remaining modes, except for F, the frequencies do not match, although the mean amplitudes are close.

From these results, no clear links can be identified between the frequency/amplitude, the shallowness and the ability of the numerical model to reproduce the flow.

Spatial modes

One of the stakes in this article is to verify whether 2D-H shallow water equations can reproduce the flow patterns observed within the reservoir. We choose to characterise these flow patterns using the vorticity contours of the spatial modes calculated with Eq. 5 as described by Peltier *et al.* (2014b).

Figure 3 represents the vorticity fields of the mode 1 (exp. and num.) and mode 3 (num.)/4 (exp.) for each flow-case. The physical difference between $m = 1$ and $m = 3$ can be found in Peltier *et al.* (2014b). The paired modes 1 and 2 are the expression of a convective instability called sinuous, which is responsible for the meandering of the jet, while modes 3 and 4 are the expression of an instability called varicose, which is responsible for the local mixing. The opposite sign of the vortical structures as k_s increases for a given POD mode

must be related to the POD transformation and to the correlation matrix of the velocity (see appendix), which can slightly differ from one simulation to another. When the eigenvalue problem is solved for finding the modes, the modes are ranked by decreasing value of the eigenvalues. When POD modes are paired, the spatial mode of $m = i+1$ is always opposite to the one of $m = i$ so as it can be seen for the temporal coefficients. Depending on the simulation, the eigenvalue corresponding to a sign of the spatial mode can be larger or smaller than the eigenvalue corresponding to the opposite spatial mode. Regarding the breakdown of the structures for the modes 3 and 4, it may be related to the influence of the bottom friction and therefore of the bottom generated turbulence, which prevent the lateral spreading of the structures.

The comparison of the numerical results with experiments emphasizes that in mode 1 the small upstream vortices, located symmetrically on either sides of the reservoir centreline, are well represented by the model. In the sequel, the emergence of the large counter vortices occurs at almost the same streamwise distance and the width of the patterns is well reproduced. On the other hand, the streamwise distribution differs in terms of number of vortical structures. In the simulation, the number of vortices is higher than in experiments. This difference decreases with decreasing friction number (from F to NF). This discrepancy between simulations and experiments may be attributed to the inability of the shallow water equations to reproduce three-dimensional structures. For high friction numbers (*i.e.* frictional regime), the length scales of the structures developing in the reservoir are of the same order as the water depth and are therefore three-dimensional. In contrast, when the friction number is decreased, mainly horizontal structures develop in the flow and they are more easily rendered by the shallow water equations.

For the vorticity distribution of mode 3/4 no clear trend between the shallowness and the shape of the vortical structures is identified. Nevertheless the width of the vortical zone is

globally well rendered and the results are consistent with those presented in subsection "*temporal coefficients*" in terms of frequency (Table 2). Indeed, in the flow cases where the computed frequencies overestimate the experimental ones (FT and NF for modes 3/4 and 4/5), the spatial scale of the vortical structures obtained here are smaller than those experimentally observed (Figure 3). The opposite is also observed in the case where the computed frequencies underestimate the experimental ones (Figure 3).

From the previous observations, it results that the first two modes are relatively well represented by the numerical model. In contrast, the numerical model does not succeed in representing the less energetic modes 3 and 4. This may have an incidence on the estimation of the momentum transfer within the jet.

Energy

By construction, the mth eigenvalue obtained from the resolution of Eq. (3) corresponds to the mean fluctuating kinetic energy per unit mass captured by the mth mode, E_m, and the sum of all non-zero eigenvalues is equal to the total mean fluctuating kinetic energy per unit mass, E_T.

The mean fluctuating kinetic energy per mode was calculated for each case and is represented in Figure 4. In Figure 5, the sum of the mean fluctuating kinetic energy of the ten first modes, E_{10}, is given as an indicator of the ability of the numerical model to represent the energy of the dominant modes and the contribution of the first five modes is displayed. In each figure, the results were normalised by the square of the inlet velocity (U^2_{in}), which reflects the mean kinetic energy injected in the flume. For all cases, the two first modes are well paired in term of energy, which is consistent with the previous observations made for the temporal coefficients and spatial modes (subsections "temporal coefficients" and "*spatial*

modes"). The mean fluctuating kinetic energy of the modes 1 and 2 is reproduced with an error ranging between -56 % and 65 %.

When looking at the energy of the higher modes, the ratio E_m/U^2_{in} in the Frictional case (F) is reasonably well represented up to $m = 30$, with however some overestimations for the first ten modes. This leads to an overestimation by 77% of the ratio E_{10}/U^2_{in} (Figure 5). For the transition case FT, the first four modes are very well represented (very slight overestimation), the others being underestimated. Nevertheless the energy of the dominant modes is well captured, as E_{10}/U^2_{in} is only 13% higher than in the experiment. This is consistent with the property of the first modes to contain most of the flow energy (Figure 5). For the transition case NFT, the three first modes are underestimated and the next three are overestimated, leading to an underestimation of E_{10}/U^2_{in} by 41% compared to the experiment, as the first two modes are dominant in the overall flow energy. Finally for the non-frictional case, the first two modes are well represented, while modes 3 and 4 are underestimated E_{10}/U^2_{in} being underestimated by 26%.

As shown by these results, the numerical model succeeds in capturing the energy of the first two modes, which are overwhelmingly dominant for such flows (Figure 5) (Peltier *et al.*, 2014b). In the sequel, the number of modes, for which the energy is well represented, decreases with the friction number (i.e. with decreasing shallowness).

Discussion

In most operational numerical models, the roughness height in the friction formula is the main adjustable parameter. Hence, in this section, we discuss the influence of the roughness height on the numerical results and we identify the possible causes of differences with the experiments.

Additional simulations were performed with $k_s = 0.1$ mm (mildly rough) and $k_s = 1$ mm (rough). The results are all included in the previous figures and the percentages of relative differences with experiments are detailed in Table 3 for E_{10}, f_m, $<|a_m|>$ and the four first modes of E_m.

Energy

For F and FT, increasing the roughness height enables a better description of the energy in the two first modes (see $k_s = 1$ mm in Table 3). This trend is also observed for the third and the fourth modes to a lesser extent. These results are confirmed by the sum of the mean fluctuating kinetic energy of the ten first modes (E_{10}): the relative difference with experiments reveals a net dependence on the roughness height. These results emphasize the role of the friction in such shallow flows (S > 0.1). For NFT and NF, this tendency is less clear, whatever the modes. This tends to confirm that the friction is not the only effect that affects the flow development.

Temporal coefficients

For the frequency and the mean amplitude, the variation of the roughness height significantly impacts the first and second modes of the transitional flow NFT and NF. In these cases, increasing the roughness improves the matching between numerical modelling and experiments. In contrast the roughness height has little effect on the frequency in the frictional case F, which suggests that base friction is dominant here. This differs from Babarutsi *et al.* (1996), who suggested that in the case of a sudden expansions with shallow recirculating flow, the friction is the dominant process for S > 0.1 and the diffusion (turbulence) only affects the transport of scalar. Here, the difference in the flow case F may be attributed to the influence of the viscosity on the development of the structures, as the Reynolds number in this case is particularly small (R = 4,766, Table 1). This difficulty is a

direct consequence of the experimental set-up and would not be encountered in real-scale applications. Regarding the frequency and the mean amplitude of the next modes, a significant improvement is obtained for the NFT and NF flow-cases when k_s is increased. For the flow-case F, the higher value of k_s reduces the agreement with the experimental frequencies, but such a high value of k_s is relatively unrealistic for our experimental set-up and should be considered here as an upper bound for our sensitivity analysis. For the flow-case FT, changing k_s has no effect; but in both F and FT cases, the mean amplitudes are improved when k_s is increased.

Spatial modes

The shapes of the spatial modes are finally analysed (Figure 3). The streamwise evolution of the vortical structures in modes 1 (and 2, since they are paired) reveals no significant change for the flow-cases F and FT when increasing k_s. This is due to the viscous effect mentioned above, which prevents the structures to laterally spread. In contrast, for NFT, the structures become larger and are very close to the experimental ones for $k_s = 1$ mm, whereas for NF the longitudinal size of the vortical structures decreases as k_s increases and get close to the experiment ones. This finding is also consistent with the influence of the roughness height on the frequencies. For NFT the frequencies of the first and second modes were initially overestimated, while they become better estimated as k_s increases, together with an increase in the size of the vortical structures. *Vice-versa* is obtained for NF, the computed frequencies are increased and the length-scale of the vortices decreases as k_s is increased. This result highlights the complicated balance between the bottom generated structures and the large horizontal structures that develop for $S < 0.1$. Nevertheless, it is clear that the vertical length-scale, linked to the bottom generated turbulence, affects the development of large structures, by preventing them to spread. For the next modes, no big differences are observed for F and FT. Similar types of patterns are obtained for all three values of k_s, but the

matching with experiments remains imperfect, consistently, the corresponding frequencies where not changed as k_s was varied. In contrast, increasing k_s for NFT and NF enables to obtain patterns, which are very close to the experimental ones. The computation of the corresponding frequencies was also strongly improved by an increase in the roughness height. These results show that the flows, even when S is small, are still partly controlled by the bottom generated turbulence, i.e. by the vertical length-scale.

The difference in large pattern shapes can be explained by the fact that the use of the standard coefficients (for unconfined three-dimensional flows) in the k-ε model can induce an inappropriate estimation of the turbulent exchanges in the flow at small S (Chu *et al.*, 2004). For NF, S is equal to 0.03 and the coherent structures mostly depend on the geometry of the reservoir (Peltier *et al.*, 2014a): they are mainly horizontal, several times larger than the water depth and highly energetic. The non-isotropic behaviour of the structures cannot be plainly represented by the turbulence model used. On the other hand at low discharge (F), S = 0.18 and the coherent structures are constrained by the shallowness of the flow, their size being of the same order of magnitude as the water depth. For this flow configuration, the k-ε model has less influence, as the relative importance of the turbulence generated by the bottom is higher.

Link between friction and turbulence

An analysis of the relative importance of the horizontal and vertical turbulent length-scales has been performed by comparing the computed values of the eddy viscosity $v_{T,2D}$ related to the horizontal turbulent mixing and of the eddy viscosity $v_{T,3D}$ related to the vertical turbulent mixing (notations consistent with Erpicum *et al.* (2009)). $v_{T,3D}$ is mostly of the same order of magnitude as the kinematic viscosity of water v, whereas $v_{T,2D}$ is generally two to three orders of magnitude higher than v. Since in all configurations the mean values of $v_{T,3D}$

do not exceed 2 % of the mean values of $\nu_{T,2D}$, the influence of the vertical mixing is then significantly lower than the horizontal one. Nonetheless, it has an influence on the small structures developing in the jet. This is due to the fact that the largest values of $\nu_{T,3D}$ are located in the centre of the main jet, where absolute flow velocities are the highest and these values increase with increasing k_s. In contrast, the largest values of $\nu_{T,2D}$ extend over the recirculation zones, confirming that $\nu_{T,2D}$ plays by far a major part in the modelling of the flow mixing between the jet and the recirculations, but has less influence in the generation of structures within the jet. When comparing sequentially configurations F, FT, NFT and NF, the relative valued of $\nu_{T,3D}$ compared to $\nu_{T,2D}$ decreases monotonously from one configuration to the next.

Conclusion

In the present study, the capability of a two-dimensional shallow water numerical model to simulate meandering flows in shallow rectangular reservoirs was investigated. Numerical simulations were based on four experiments, in which the water depth was varied to assess the effect of the shallowness of the flow on the quality of the simulations. A k-ε turbulent closure accounting for horizontal and vertical length-scales was used in order to free us of any calibration. The Colebrook-White friction formula was used, in which the roughness height was the only parameter to be adjusted as it is often the case in operational numerical models for engineering practice. Three roughness heights were therefore considered: smooth ($k_s = 0$ mm), mildly rough ($k_s = 0.1$ mm) and rough ($k_s = 1$ mm).

As simulations are unsteady, a Proper Orthogonal Decomposition of the fluctuating velocity fields was used for describing the flow. The agreement between the numerical simulations and the experiments was analysed through six parameters: mean fluctuating kinetic energy per mode, the sum of the mean fluctuating kinetic energy in the ten first

modes, the frequency and the mean amplitude of the four first temporal coefficients, the longitudinal and lateral variation of the four first spatial modes.

As shown by comparisons between simulations assuming smooth bottom and experiments, these simulations are in relatively good agreement with the experimental observations, as far as the dominant modes of the POD (mode 1 and mode 2) are concerned and whatever is the shallowness. The numerical reproduction of the next modes is less successful, especially as regards the shape of the spatial modes. However these higher order modes contribute significantly less to the overall fluctuating kinetic energy of the flow.

Increasing the roughness height enables a better reproduction of the dominant modes and of the following modes. Nevertheless for the very shallow case, some viscous effects are detected, which hamper a good agreement between numerical and experimental results.

As a conclusion, the 2D shallow water equations are able to globally reproduce the behaviour of the meandering flows in shallow reservoirs, but show some difficulty for reproducing the exact shapes of the structures developing inside. An analysis of the influence of the coefficients involved in the turbulence model would be required, as well as a sensibility analysis with respect to the type of turbulent closure (e.g. k-ω vs. k-ε).

All experimental data are available upon request.

Acknowledgments

Notations

$a_m(t)$ = temporal coefficient of the mth POD mode [-]

$<|a_m|>$ = mean amplitude of the temporal coefficient of the mth POD mode [-]

b = width of the inlet and outlet channels [m]

B = width of the reservoir [m]

D = hydraulic radius at the reservoir inlet [m]

ΔB = width of the sudden expansion in the reservoir [m]

E_m = mean fluctuating kinetic energy per unit mass captured by the mth POD mode [m²/s²]

E_{10} = sum of the mean fluctuating kinetic energy per unit mass captured by the 10 first POD modes [m²/s²]

f = Darcy-Weisbach coefficient [-]

f_m = main frequency of the mth POD mode [Hz]

F = Froude number at the inlet [-]

g = gravity acceleration [m/s²]

H = mean water depth in the reservoir [m]

k_s = roughness height of the bed [mm]

L = length of the rervoir [m]

Q = water discharge at the inlet [m]

R = Reynolds number at the reservoir inlet [-]

S = friction number at the reservoir inlet [-]

SF = shape factor of the reservoir [-]

u_* = friction velocity [m/s]

U_{in} = mean velocity at the reservoir inlet [m/s]

x = streamwise coordinate [m]

y = spanwise coordinate [m]

z = vertical coordinate [m]

$\phi_m(x)$ = spatial mode of the mth POD mode (two components) [m/s]

ν = kinematic viscosity of water at 20°C [m²/s]

$\nu_{\text{T,2D}}$ = eddy viscosity related to the horizontal turbulent mixing [m²/s]

$\nu_{\text{T,3D}}$ = eddy viscosity related to the vertical turbulent mixing [m²/s]

References

Aloui, F., and Souhar, M. (2000). "Experimental study of turbulent asymmetric flow in a flat duct symmetric sudden expansion." Journal of Fluids Engineering, Transactions of the ASME, 122(1), 174-177.

Babarutsi, S., and Chu, V.H. (1998). "Modeling transverse mixing layer in shallow open-channel flows." Journal of Hydraulic Engineering, ASCE, 124(7), 718-727.

Babarutsi, S., Nassiri, M., and Chu, V.H. (1996). "Computation of shallow recirculating flow dominated by friction." Journal of Hydraulic Engineering, ASCE, 122(7), 367-372.

Berkooz, G., Holmes, P., and Lumley, J.L. (1993). "The proper orthogonal decomposition in the analysis of turbulent flows." Annual Review of Fluid Mechanics, 25(1), 539-575.

Brevis, W., and García-Villalba, M. (2011). "Shallow-flow visualization analysis by proper orthogonal decomposition." Journal of Hydraulic Research, 49(5), 586-594.

Camnasio, E., Orsi, E., and Schleiss, A.J. (2011). "Experimental study of velocity fields in rectangular shallow reservoirs." Journal of Hydraulic Research, 49(3), 352-358.

Camnasio, E., Pirotton, M., Erpicum, S., and Dewals, B. (2012). "Experimental and numerical investigation of a meandering jet in shallow rectangular reservoirs under different hydraulic conditions." Proc., 3rd International Symposium on Shallow Flows.

Camnasio, E., Erpicum, S., Orsi, E., Pirotton, M., Schleiss, A.J., and Dewals, B. (2013). "Coupling between flow and sediment deposition in rectangular shallow reservoirs." Journal of Hydraulic Research.

Canbazoglu, S., and Bozkir, O. (2004). "Analysis of pressure distribution of turbulent asymmetric flow in a flat duct symmetric sudden expansion with small aspect ratio." Fluid Dynamics Research, 35(5), 341-355.

Cavar, D., and Meyer, K.E. (2012). "LES of turbulent jet in cross flow: Part 2 - POD analysis and identification of coherent structures." International Journal of Heat and Fluid Flow, 36, 35-46.

Chen, D., and Jirka, G.H. (1999). "LIF study of plane jet bounded in shallow water layer." Journal of Hydraulic Engineering, 125(8), 817-826.

Chu, V.H., and Babarutsi, S. (1988). "Confinement and bed-friction effects in shallow turbulent mixing layers." Journal of Hydraulic Engineering, ASCE, 114(10), 1257-1274.

Chu, V.H., Khayat, R.E., and Wu, J.H. (1983). "Stability of turbulent shear flows in shallow channel." Proc., 20th IAHR Congr., Sep. 5-9, Moscow, USSR, Delft, The Netherlands, IAHR, 128-133.

Chu, V.H., Liu, F., and Altai, W. (2004). "Friction and confinement effects on a shallow recirculating flow." Journal of Environmental Engineering and Science, 3(5), 463-475.

Couplet, M., Sagaut, P., and Basdevant, C. (2003). "Intermodal energy transfers in a proper orthogonal decomposition - Galerkin representation of a turbulent separated flow." Journal of Fluid Mechanics, 491, 275-284.

Dewals, B., Kantoush, S.A., Erpicum, S., Pirotton, M., and Schleiss, A.J. (2008). "Experimental and numerical analysis of flow instabilities in rectangular shallow basins." Environmental Fluid Mechanics, 8(1), 31-54.

Dufresne, M., Dewals, B.J., Erpicum, S., Archambeau, P., and Pirotton, M. (2010a). "Experimental investigation of flow pattern and sediment deposition in rectangular shallow reservoirs." International Journal of Sediment Research, 25(3), 258-270.

Dufresne, M., Dewals, B.J., Erpicum, S., Archambeau, P., and Pirotton, M. (2010b). "Classification of flow patterns in rectangular shallow reservoirs." Journal of Hydraulic Research, 48(2), 197-204.

Dufresne, M., Dewals, B.J., Erpicum, S., Archambeau, P., and Pirotton, M. (2011). "Numerical investigation of flow patterns in rectangular shallow reservoirs." Engineering Applications of Computational Fluid Mechanics, 5(2), 247-258.

Dufresne, M., Dewals, B., Erpicum, S., Archambeau, P., and Pirotton, M. (2012). "Flow patterns and sediment deposition in rectangular shallow reservoirs." Water and Environment Journal, 26(4), 504-510.

Erpicum, S., Dewals, B.J., Archambeau, P., and Pirotton, M. (2010). "Dam break flow computation based on an efficient flux vector splitting." Journal of Computational and Applied Mathematics, 234(7), 2143-2151.

Erpicum, S., Meile, T., Dewals, B.J., Pirotton, M., and Schleiss, A.J. (2009). "2D numerical flow modeling in a macro-rough channel." International Journal for Numerical Methods in Fluids, 61(11), 1227-1246.

Foss, J.F., and Jones, J.B. (1968). "Secondary Flow Effects in a Bounded Rectangular Jet." Journal of Basic Engineering, 90(2), 241-248.

Hauet, A. (2009). "Discharge estimate and velocity measurement in river using Large-Scale Particle Image Velocimetry; Estimation de débit et mesure de vitesse en rivière par Large-Scale Particle image Velocimetry." La Houille Blanche(1), 80-85.

Hauet, A., Kruger, A., Krajewski, W.F., Bradley, A., Muste, M., Creutin, J.D., and Wilson, M. (2008). "Experimental system for real-time discharge estimation using an image-based method." Journal of Hydrologic Engineering, 13(2), 105-110.

Holdeman, J.D., and Foss, J.F. (1975). "The Initiation, Development, and Decay of the Secondary Flow in a Bounded Jet." Journal of Fluids Engineering, 97(3), 342-352.

Holmes, P., Lumley, J.L., Berkooz, G., and Rowley, C.W. (2012). Turbulence, Coherent Structures, Dynamical Systems and Symmetry. Second Edition, Cambridge University Press.

Kantoush, S.A. (2008). "Experimental study on the influence of the geometry of shallow reservoirs on flow patterns and sedimentation by suspended sediments." Ph. D. Ph. D. thesis, EPFL, Lausanne.

Kantoush, S.A., De Cesare, G., Boillat, J.L., and Schleiss, A.J. (2008). "Flow field investigation in a rectangular shallow reservoir using UVP, LSPIV and numerical modelling." Flow Measurement and Instrumentation, 19(3-4), 139-144.

Khan, S., Melville, B.W., Shamseldin, A.Y., and Fischer, C. (2013). "Investigation of flow patterns in storm water retention ponds using CFD." Journal of Environmental Engineering, 139(1), 61-69.

Le Coz, J., Hauet, A., Pierrefeu, G., Dramais, G., and Camenen, B. (2010). "Performance of image-based velocimetry (LSPIV) applied to flash-flood discharge measurements in Mediterranean rivers." Journal of Hydrology, 394(1-2), 42-52.

Mariotti, G., Falcini, F., Geleynse, N., Guala, M., Sun, T., and Fagherazzi, S. (2013). "Sediment eddy diffusivity in meandering turbulent jets: Implications for levee formation at river mouths." Journal of Geophysical Research: Earth Surface, 118(3), 1908-1920.

Mullin, T., Shipton, S., and Tavener, S.J. (2003). "Flow in a symmetric channel with an expanded section." Fluid Dynamics Research, 33(5-6), 433-452.

Oca, J., and Masaló, I. (2007). "Design criteria for rotating flow cells in rectangular aquaculture tanks." Aquacultural Engineering, 36(1), 36-44.

Peltier, Y., Erpicum, S., Archambeau, P., Pirotton, M., and Dewals, B. (2013). "Experimental and numerical investigation of meandering jets in shallow reservoir: potential impacts on deposit patterns." THESIS 2013, Two-pHase modElling for Sediment dynamIcs

in Geophysical Flows, K.D. Nguyen, M. Benoit, S. Guillou, N. Sheibani, J.G. Philipps, and D. Pham Van Bang, eds., SHF - EDF R&D, Chatou, France.

Peltier, Y., Erpicum, S., Archambeau, P., Pirotton, M., and Dewals, B. (2014a). "Experimental investigation of meandering jets in shallow reservoir." Environmental Fluid Mechanics, 14(3), 699-710.

Peltier, Y., Erpicum, S., Archambeau, P., Pirotton, M., and Dewals, B. (2014b). "Meandering jets in shallow rectangular reservoirs: POD analysis and identification of coherent structures." Experiments in Fluids, 55(6), 1-16.

Peng, Y., Zhou, J.G., and Burrows, R. (2011). "Modeling free-surface flow in rectangular shallow basins by using lattice boltzmann method." Journal of Hydraulic Engineering, 137(12), 1680-1685.

Perrin, R., Braza, M., Cid, E., Cazin, S., Barthet, A., Sevrain, A., Mockett, C., and Thiele, F. (2007). "Obtaining phase averaged turbulence properties in the near wake of a circular cylinder at high Reynolds number using POD." Experiments in Fluids, 43(2-3), 341-355.

Rempfer, D., and Fasel, H.F. (1994). "Evolution of three-dimensional coherent structures in a flat-plate boundary layer." Journal of Fluid Mechanics, 260, 351-375.

Roache, P.J. (1994). "Perspective: a method for uniform reporting of grid refinement studies." Journal of Fluids Engineering, Transactions of the ASME, 116(3), 405-413.

Rowland, J.C., Stacey, M.T., and Dietrich, W.E. (2009). "Turbulent characteristics of a shallow wall-bounded plane jet: Experimental implications for river mouth hydrodynamics." Journal of Fluid Mechanics, 627, 423-449.

Sirovich, L. (1987). "Turbulence and the dynamics of coherent structures. PART I: coherent structures." Quarterly of Applied Mathematics, 45(3), 561-570.

Stovin, V.R., and Saul, A.J. (2000). "Computational fluid dynamics and the design of sewage storage chambers." Journal of the Chartered Institution of Water and Environmental Management, 14(2), 103-110.

Proper Orthogonal Decomposition: snapshot method

A short description of the snapshot method used on the fluctuating velocity fields of this study and coded in Matlab[©] (Peltier *et al.*, 2014b) is presented here.

$\{u(x,t_1), u(x,t_2),...,u(x,t_N)\}$ is a collection of N ($N \in \mathbb{N}$) instantaneous horizontal velocity fields, with $\Delta t = t_{n+1} - t_n = CST$ ($n<N$)and $x \in \Omega \subset \mathbb{R}$. Each velocity is called "snapshot". Each snapshot is a square integrable function ($u(x,t_n) \in L^2(\Omega)$) and can be split into a steady part, $\langle u(x,t_n) \rangle_N$ and a fluctuating part, $u'(x,t_n)$, with $\langle \ \rangle_N$ the operator of ensemble average over the N snapshots.

The aim of the POD is to decompose $u'(x,t_n)$ into an orthonormal basis of M spatial function $\phi_m(x)$ of $L^2(\Omega)$, called spatial modes, and an orthogonal basis of M temporal coefficients, $a_m(t_n)$ ($n \in \{1, ..., N\}$, $m \in \{1, ..., M \leq N\}$ M and $N \in \mathbb{N}$), such that:

$$\min\left(\frac{1}{N} \sum_{n=1}^{N} \left\| u'(x,t_n) - \sum_{m=1}^{M \leq N} a_m(t_n)\phi_m(x) \right\|_{L^2}^2 \right) \tag{1}$$

$\| \ \|_{L^2} = \sqrt{(\ , \ )_{L^2}}$ being the induced norm in $L^2(\Omega)$ and $(\ , \ )_{L^2}$ the inner product for $L^2(\Omega)$.

The snapshot method proceeds in three steps:

1. It first requires the calculation of the temporal correlation matrix C:

$$C_{ij} = \sum_{k=1}^{P} u'\left(x_p,t_i\right) W_{kk} u'\left(x_p,t_j\right), C \in \mathbb{R} \qquad \mathbb{R} \tag{2}$$

W being a diagonal weighting matrix, for which the elements along the diagonal are the cell volumes of each of the P grid points of one snapshot.

2. The temporal coefficients $a_m(t)$ are secondly deduced from the resolution of the eigenvalue problem that follows:

$$\frac{1}{N}\sum_{j=1}^{N}C_{ij}\alpha_m(t_j) = \lambda_m\alpha_m(t_i)$$

(3)

As C is definite, positive and symmetric, the eigenvalues λ_m are all real with $\lambda_1 \geq \lambda_2 \geq ... \geq \lambda_N > 0$, and the eigenvectors $\alpha_m(t)$ are orthonormal. The temporal coefficients, $a_m(t)$, are a function of the eigenvectors and of the eigenvalues and they are orthogonal:

$$a_m(t) = \sqrt{N\lambda_m}\,\alpha_m(t), \text{ with } \langle a_n \rangle_N = 0 \text{ and } \langle a_n a_m \rangle_N = \lambda_n\delta_{nm}$$

(4)

3. The spatial modes are finally computed by projecting the fluctuating velocity ensemble onto the temporal coefficients, *i.e.*:

$$\phi_m(x) = \frac{1}{N\lambda_m}\sum_{n=1}^{N}u'(x,t_n)a_m(t_n), \text{ with } \|\phi_m\|_{L^2}^2 = \phi_m^T W \phi_m = 1$$

(5)

The spatial modes are orthonormal with respect to the inner product in L^2, $\phi_m^T W \phi_m$.

Table 1: Main characteristics of the measured flows.

Test ID	Q (L/s)	H (cm)	F	R	S	Friction regime
F	0.125	1.25	0.36	4,766	0.18	Frictional
FT	0.250	1.80	0.41	8,456	0.10	Frictional close Transition
NFT	0.500	2.75	0.44	1,4878	0.06	Non-Frictional close Transition
NF	1.000	4.20	0.46	2,4267	0.03	Non-Frictional

Table 2: Frequencies, f_m, and mean amplitude, $<|a_m(t)|>_t$, of the mth temporal coefficient in the POD analysis.

		F				FT				NFT				NF			
	m / k_s	1	2	3	4	1	2	3	4	1	2	3	4	1	2	3	4
f_m (Hz) *	Exp	0.17	0.17	0.10	0.08	0.21	0.21	0.22	0.22	0.27	0.27	0.55	0.55	0.48	0.48	0.34	0.34
	0	0.26	0.26	0.07	0.07	0.22	0.22	0.43	0.43	0.38	0.38	0.11	0.11	0.34	0.34	0.69	0.69
	0.1	0.25	0.25	0.07	0.07	0.22	0.22	0.43	0.43	0.38	0.38	0.75	0.75	0.47	0.47	0.14	0.14
	1	0.25	0.25	0.03	0.03	0.22	0.22	0.43	0.43	0.27	0.27	0.54	0.54	0.47	0.47	0.14	0.14
$<|a_m|>_t \times 10^3$ (-) *	Exp	4	4	2	2	9	9	2	2	17	16	4	4	15	14	6	6
	0	6	5	3	3	11	10	3	3	11	10	6	6	17	16	5	5
	0.1	6	5	3	3	11	10	3	3	17	13	3	3	13	12	7	7
	1	5	4	3	3	11	10	3	2	15	14	5	5	15	13	6	6

* Numerical modes 1 and 2 are compared with experimental modes 1 and 2, while numerical modes 3 and 4 are compared with experimental modes 4 and 5.

Table 3: Relative difference in percentage between numerical results and experiments for E_m, E_{10}, f_m and $<|a_m|>$.

		F				FT				NFT				NF			
	m \ k_s	1	2	3	4	1	2	3	4	1	2	3	4	1	2	3	4
E_m^*	0	63	65	150	182	38	33	56	47	-56	-52	95	110	11	4.8	-46	-51
	0.1	70	67	145	181	37	32	54	42	-3	-26	-48	-44	-27	-29	-3	-4.9
	1	22	16	148	141	26	28	6	-25	-18	-21	7.8	18	-13	-23	-14	-18
E_{10}	0		77				13				-41				-26		
	0.1		81				12				-30				-29		
	1		46				2				-31				-25		
f_m^*	0	49		-17		1		101		39		-80		-28		103	
	0.1	48		-19		1		101		38		38		0		-59	
	1	47		-70		1		100		-1		-1		0		-59	
$<|a_m|>^*$	0	35		80		17		34		-35		51		9		-19	
	0.1	37		76		16		33		-7		-21		-15		10	
	1	15		73		13		3		-10		13		-7		3	

[*] Numerical modes 1 and 2 are compared with experimental modes 1 and 2, while numerical modes 3 and 4 are compared with experimental modes 4 and 5 (cf. subsection "*temporal coefficients*").
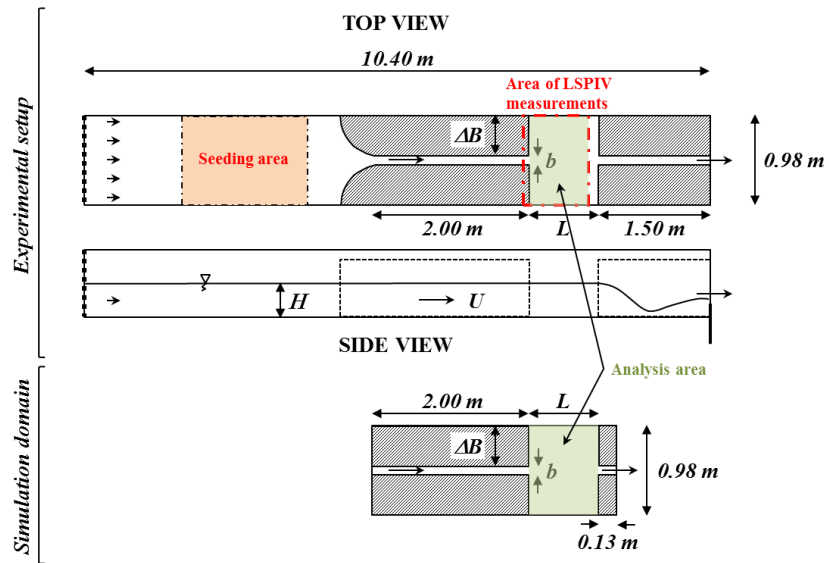
Figure 1: Sketches of the experimental device and simulation domain.
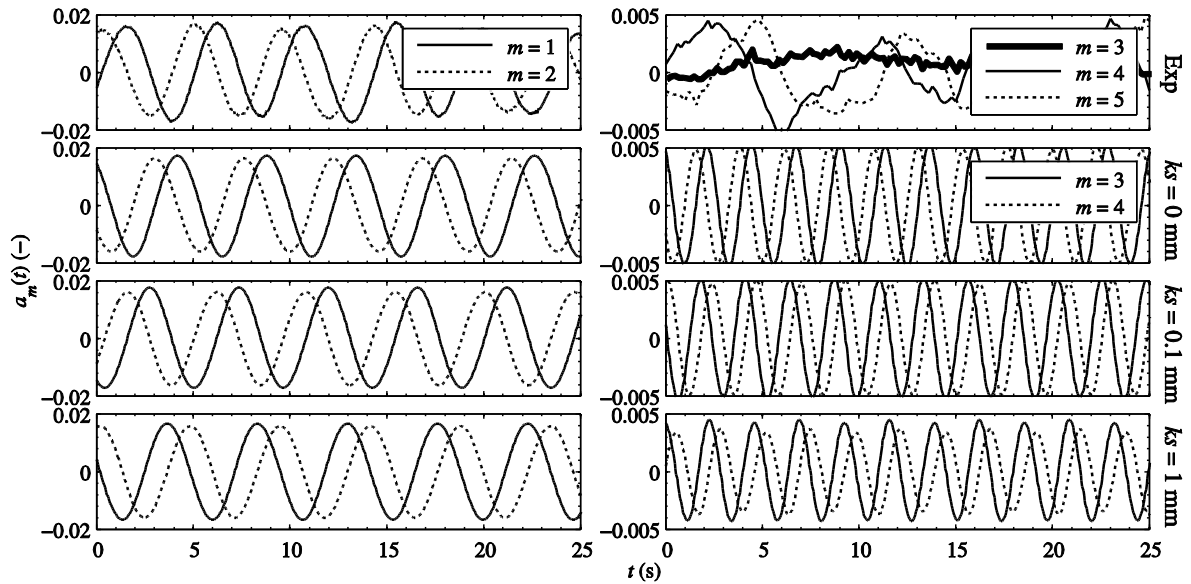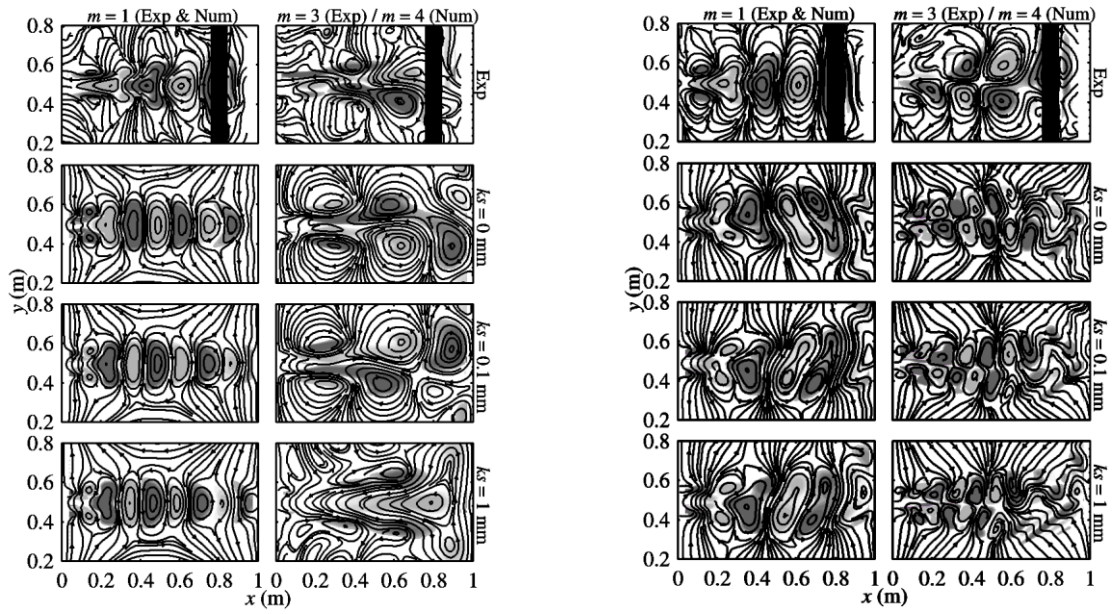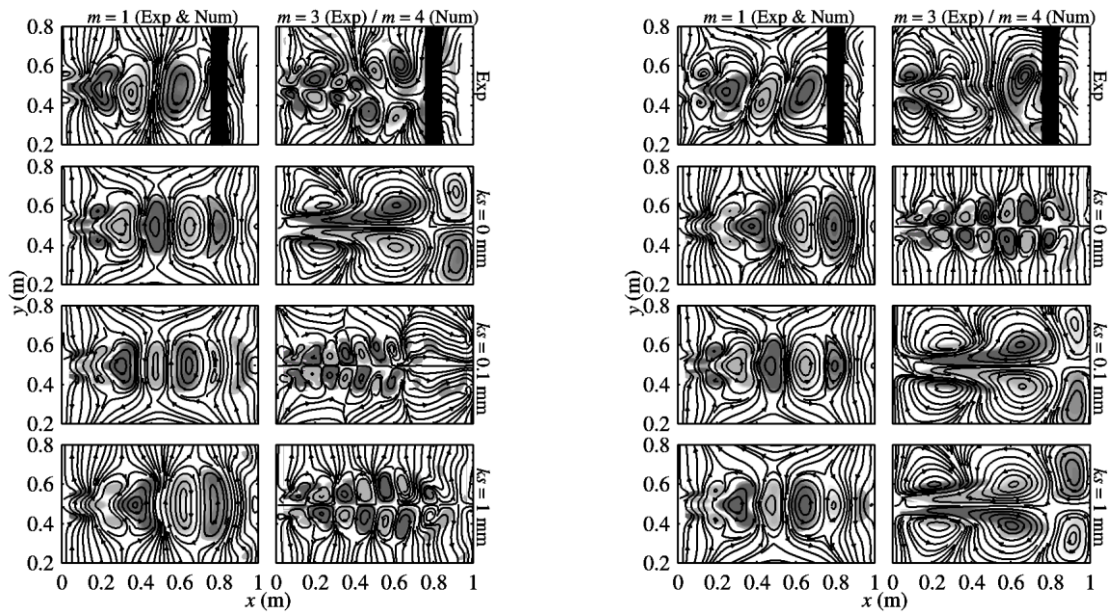

Figure 2: Temporal coefficients for FT-case. Comparison between experiment and numerical modelling.

(a) F

(b) FT

(c) NFT

(d) NF

Figure 3: Vorticity contours and streamlines of spatial modes. The black zone in the upper figures corresponds to an absence of measurements in experiments. The same grey-scale is used for all flow-cases (dark grey: vorticity < 0, white: vorticity = 0, light grey: vorticity > 0) and the grey intensity is proportional to the vorticity intensity.

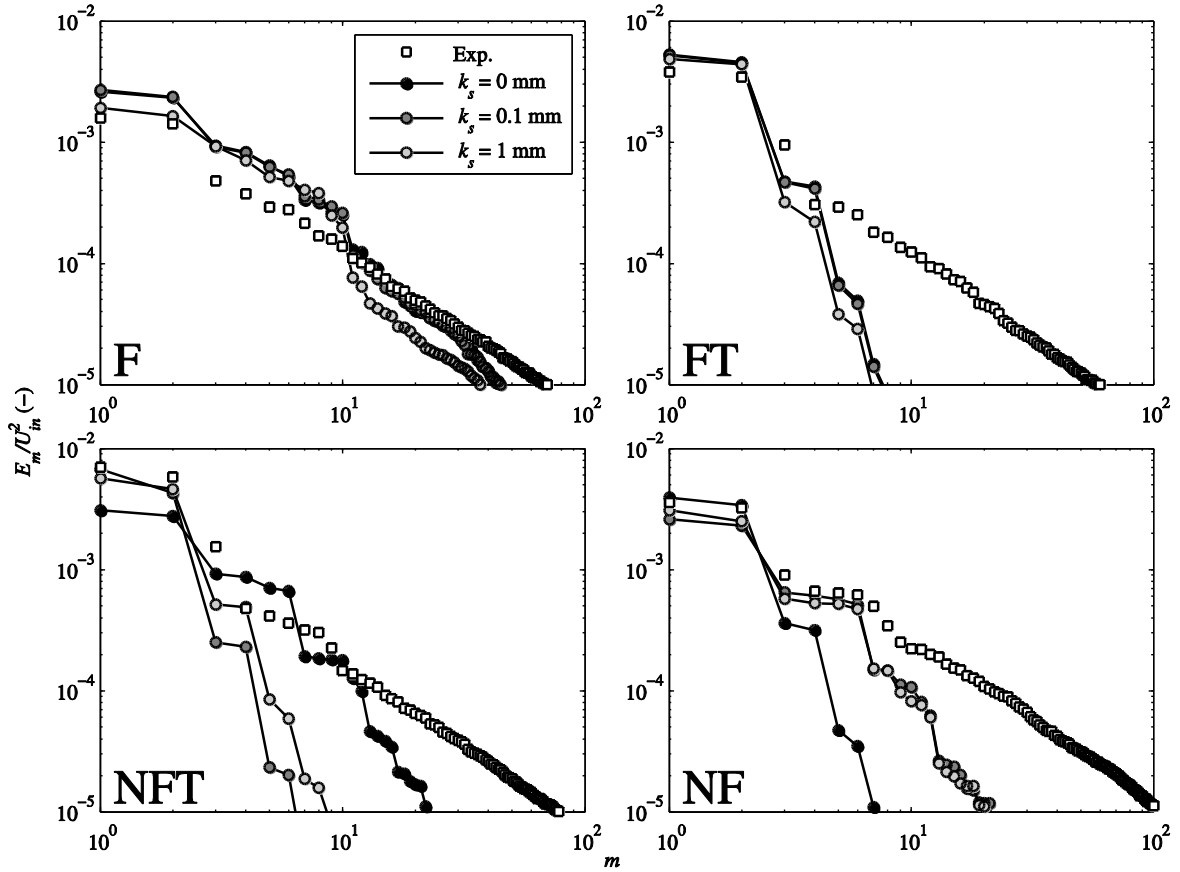Figure 4: Mean fluctuating kinetic energy contained in the mth mode and normalised by their corresponding mean kinetic energy at the inlet (U^2_{in}) for each flow-case.
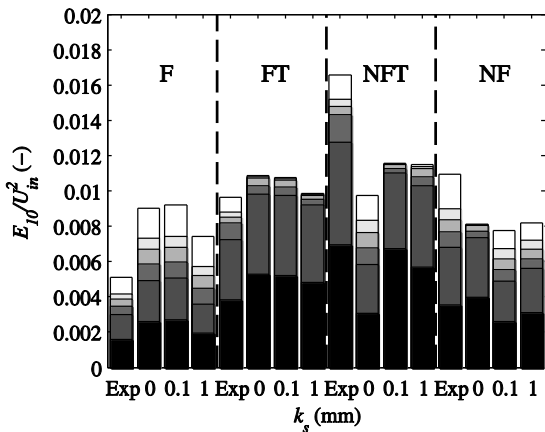

Figure 5: Sum of the mean fluctuating kinetic energy of the ten first modes, E_{10}, normalised for each flow-case by their corresponding mean kinetic energy at the inlet (U^2_{in}). The black area corresponds to the contribution of the first mode. The white area corresponds to the cumulated contributions of $m = 6$ to $m = 10$. The grey areas correspond to $m = 2$ (dark grey) to $m = 5$ (lighter grey).